

Dinuclear Fluoride Single-Bridged Lanthanoid Complexes as Molecule Magnets: Unprecedented Coupling Constant in a Fluoride-Bridged Gadolinium Compound

Julio Corredoira-Vázquez, Cristina González-Barreira, Matilde Fondo,* Ana M. García-Deibe, Jesús Sanmartín-Matalobos, Silvia Gómez-Coca, Eliseo Ruiz, and Enrique Colacio



Cite This: *Inorg. Chem.* 2022, 61, 9946–9959



Read Online

ACCESS |



Metrics & More

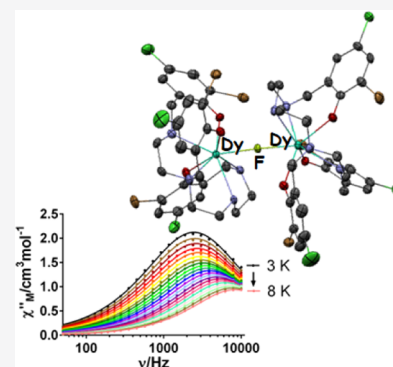


Article Recommendations



Supporting Information

ABSTRACT: A new synthetic method allows isolating fluoride-bridged complexes $\text{Bu}_4\text{N}\{[\text{M}(\text{3NO}_2, 5\text{Br-H}_3\text{L}^{1,1,4})_2(\mu\text{-F})]\}$ ($\text{M} = \text{Dy}$, 1; $\text{M} = \text{Ho}$, 2; $\text{M} = \text{Gd}$, 3) and $\text{Bu}_4\text{N}\{[\text{Dy}(\text{3Br}, 5\text{Cl-H}_3\text{L}^{1,2,4})_2(\mu\text{-F})]\cdot 2\text{H}_2\text{O}$, 4·2H₂O. The crystal structures of 1·5CH₃C₆H₅·2·2H₂O·0.75THF, 3, and 4·2H₂O·2THF show that all of them are dinuclear compounds with linear single fluoride bridges and octacoordinated metal centers. Magnetic susceptibility measurements in the temperature range of 2–300 K reveal that the Gd^{III} ions in 3 are weakly antiferromagnetically coupled, and this constitutes the first crystallographically and magnetically analyzed gadolinium complex with a fluoride bridge. Variable-temperature magnetization demonstrates a poor magnetocaloric effect for 3. Alternating current magnetic measurements for 1, 2, and 4·2H₂O bring to light that 4·2H₂O is an SMM, 1 shows an SMM-like behavior under a magnetic field of 600 Oe, while 2 does not show relaxation of the magnetization even under an applied magnetic field. In spite of this, 2 is the first fluoride-bridged holmium complex magnetically analyzed. DFT and *ab initio* calculations support the experimental magnetic results and show that apparently small structural differences between 1 and 4·2H₂O introduce important changes in the dipolar interactions, from antiferromagnetic in 1 to ferromagnetic in 4·2H₂O.



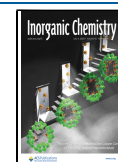
INTRODUCTION

Research in the field of lanthanoid molecular magnets has increased markedly since Rinehart and Long published their electrostatic model that explains how to boost magnetic anisotropy.¹ According to this theory, oblate ions, like Dy^{III} and Ho^{III}, maximize their anisotropy when they are in a crystal field for which the ligand electron density is concentrated above and below the *xy* plane. Therefore, oblate ions in axial fields, like linear, trigonal bipyramidal (tbp), or pentagonal bipyramidal (pbp), should give rise to molecular magnets with improved properties. Consequently, the single-molecule magnet (SMM) with the highest blocking temperature ($T_B = 80$ K) reported to date is a pseudo-linear Dy^{III} metallocene,² although a dinuclear mixed-valent dysprosium compound has recently been described that appears to match this T_B .³ However, these metallocenes are unstable in air, and compounds with other axial geometries, like pbp, could constitute a good alternative in the search for SMMs with high blocking temperatures. In fact, the T_B record (36 K) for an air-stable SMM is held by [Dy(bmbpen-F)Br] ($\text{H}_2\text{bmbpen-F} = N,N'$ -bis(5-methyl-2-hydroxybenzyl)- N,N' -bis(5-fluoro-2-methylpyridyl)ethylene diamine),⁴ a mononuclear complex with Dy^{III} in a pbp environment. Nevertheless, the geometric axis and the anisotropy axis do not always coincide,^{5–8} and accordingly, many complexes with axial geometries have poor magnetic properties.

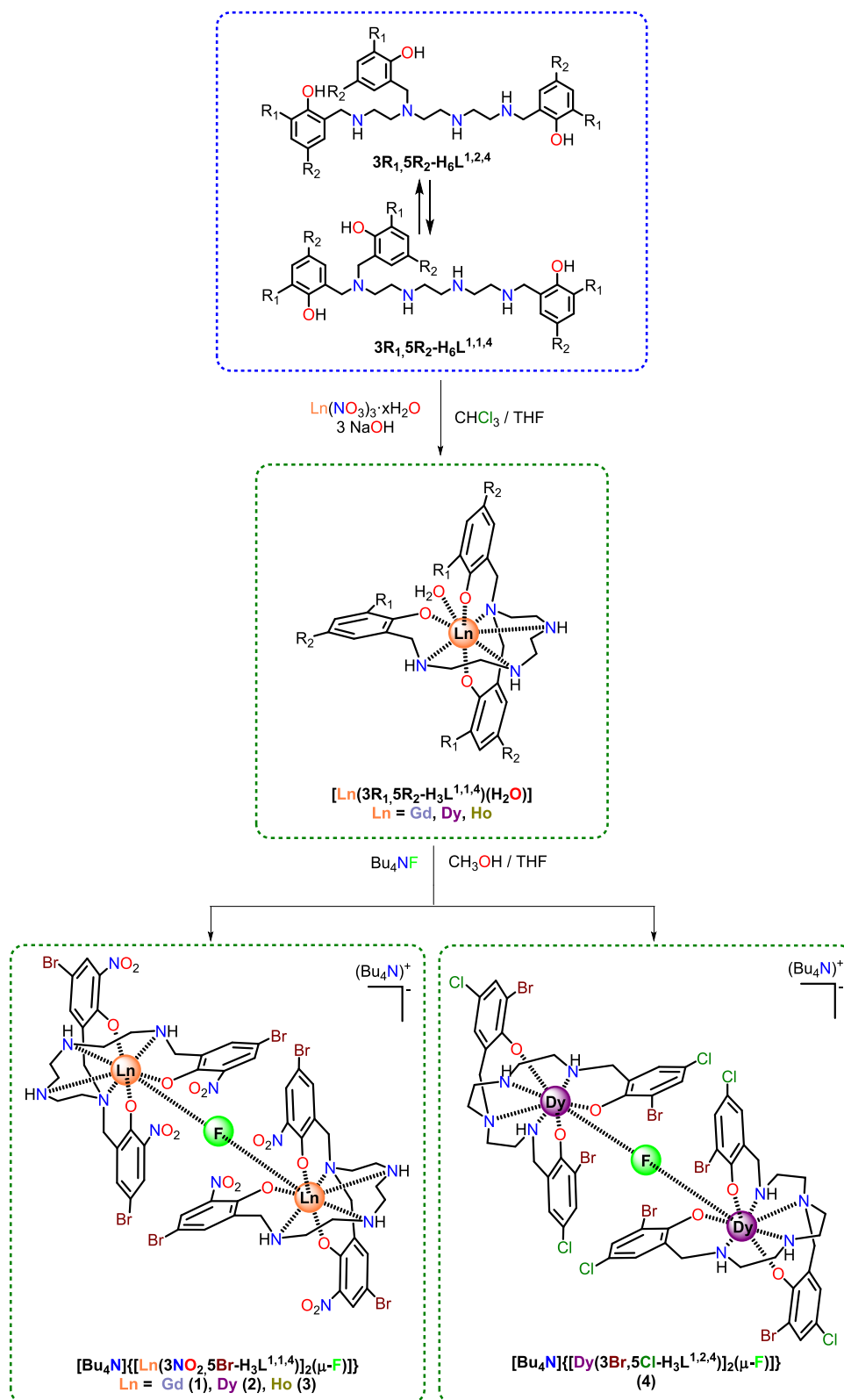
One way of ensuring axiality in lanthanoid complexes is the selective use of anionic hard donor atoms, like negatively charged oxygen or fluoride. In this way, the best results described to date were found with monodentate oxygen donors,^{9–11} and it seems that oxygen atoms from aliphatic groups provide improved axiality with respect to those from aromatic groups.^{9a} However, many of the SMMs reported with aliphatic negatively charged oxygen atoms, like alcoholates, also seem to be unstable in air.⁹ Besides, it should be noted that the Ln–O bonds should be longer than the Ln–F ones. Therefore, it seems that the use of fluoride as a ligand could be a way of maximizing the anisotropy in lanthanoid metal complexes. This idea is not new, but the synthesis of lanthanoid complexes with the fluoride ligand is, however, challenging because of the tendency of fluoride to form stable and insoluble LnF₃ compounds.¹² Thus, the number of magnetically analyzed lanthanoid metal complexes bearing fluoride as a ligand is relatively small.^{13–19} These studies point to the fact that fluoride

Received: March 8, 2022

Published: June 23, 2022



Scheme 1. Reaction Scheme for Isolation of the Fluoride-Bridged Complexes



can create strong axiality even in geometric environments that are not highly axial, such as capped square antiprism.¹⁵

With these considerations in mind, taking into account that both the synthetic routes and magnetic studies for lanthanoid complexes with fluoride ligands are still scarce, in this work, we report a successful route for the isolation of dinuclear fluoride-

bridged dysprosium, holmium, and gadolinium complexes, as well as their magnetic properties.

RESULTS AND DISCUSSION

Synthesis. All of the fluoride-bridged complexes 1–4·2H₂O were obtained by similar processes, by displacement of the water

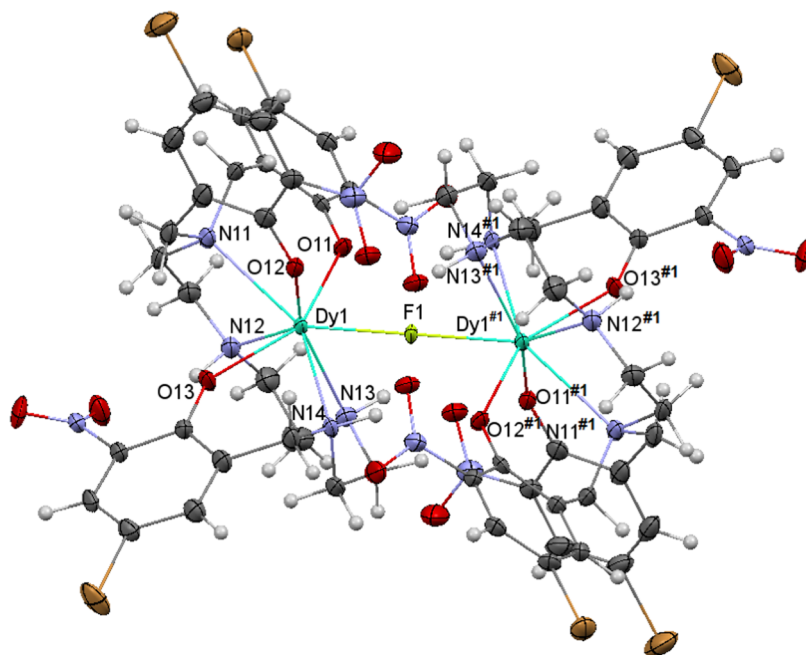


Figure 1. Ellipsoid diagram for the $\{[\text{Dy}(\text{3NO}_2, \text{5Br-H}_3\text{L}^{1,1,4})]_2(\mu\text{-F})\}^-$ anion in **1.1**.

ligand in mononuclear $[\text{M}(\text{3R}_1, \text{5R}_2\text{-H}_3\text{L}^{1,1,4})(\text{H}_2\text{O})]$ compounds²⁰ by a fluoride donor, as summarized in Scheme 1.

However, it is worth noting that, while for fluoride complexes with the $\text{3NO}_2, \text{5Br}$ substituents on the phenol rings (**1–3**), the ligand keeps its initial isomeric form (1,1,4),²⁰ for the dysprosium complex $4 \cdot 2\text{H}_2\text{O}$, with $\text{3Br}, \text{5Cl}$ as substituents on the phenol rings, the aminophenol ligand changes from the initial 1,1,4 isomer²⁰ to the final 1,2,4 one. This transformation could seem unexpected, as the equilibrium between the unsubstituted $\text{H}_6\text{L}^{1,2,4}$ and $\text{H}_6\text{L}^{1,1,4}$ species seems to displace toward the $\text{H}_6\text{L}^{1,1,4}$ isomer with increasing pH of the medium.^{21,22} Taking into account that fluoride is a basic anion, the isolation of $4 \cdot 2\text{H}_2\text{O}$ with the $[\text{3Br}, \text{5Cl-H}_3\text{L}^{1,2,4}]^{3-}$ aminophenol donor clearly indicates that the substituents on the aromatic ring play a fundamental role in the isomeric equilibrium of this kind of ligand.

The comparison of the experimental powder X-ray diffractogram of the final products with the calculated ones from single X-ray diffraction data (Figure S1) indicates that all of the complexes have been obtained with high purity, without mixtures, and that the collected samples and the solved single crystals are basically the same compounds.

The same dinuclear complexes are isolated when $[\text{M}(\text{3R}_1, \text{5R}_2\text{-H}_3\text{L}^{1,1,4})(\text{H}_2\text{O})]$ and Bu_4NF are mixed in a 1:1 or 2:1 molar ratio. However, the yield improves with the 1:1 molar ratio. Nevertheless, pure complexes with terminal fluorides could not be obtained even when this molar ratio was increased to 1:2. Despite this, it represents a systematic method to synthesize lanthanoid complexes with fluoride ligands, a task that is quite arduous, due to the strong tendency of Ln^{III} ions to form LnF_3 in the presence of fluorides.¹²

Single crystals of all of the complexes could be obtained as detailed below, allowing their single X-ray characterization. However, in spite of the multiple attempts, it was not possible to unequivocally characterize the gadolinium analogues of $4 \cdot 2\text{H}_2\text{O}$.

X-ray Diffraction Studies. The crystal structures of $\text{Bu}_4\text{N}\{[\text{Dy}(\text{3NO}_2, \text{5Br-H}_3\text{L}^{1,1,4})]_2(\mu\text{-F})\} \cdot \text{5CH}_3\text{C}_6\text{H}_5$ (**1**· $5\text{CH}_3\text{C}_6\text{H}_5$), $\text{Bu}_4\text{N}\{[\text{Ho}(\text{3NO}_2, \text{5Br-H}_3\text{L}^{1,1,4})]_2(\mu\text{-F})\} \cdot 2\text{H}_2\text{O}$ ·

0.75THF ($2 \cdot 2\text{H}_2\text{O} \cdot 0.75\text{THF}$), and $\text{Bu}_4\text{N}\{[\text{Gd}(\text{3NO}_2, \text{5Br-H}_3\text{L}^{1,1,4})]_2(\mu\text{-F})\}$ (**3**) are very similar, and they will be discussed together. The unit cell of the three complexes contains dinuclear $\{[\text{M}(\text{3NO}_2, \text{5Br-H}_3\text{L}^{1,1,4})]_2(\mu\text{-F})\}^-$ anions ($\text{M} = \text{Dy}, \text{Ho}, \text{or Gd}$) and Bu_4N^+ cations, in addition to different solvates. All of the crystals belong to the triclinic group $P\bar{1}$, and in all cases, the asymmetric unit has two chemically equal but crystallographically inequivalent halves of the molecules. Thus, each one of the two $\text{Bu}_4\text{N}\{[\text{M}(\text{3NO}_2, \text{5Br-H}_3\text{L}^{1,1,4})]_2(\mu\text{-F})\}$ complexes of the unit cell is created by an inversion center, and the crystallographically different molecules will be called X.1 and X.2 ($\text{X} = 1$ for Dy, $\text{X} = 2$ for Ho, and $\text{X} = 3$ for Gd). Ellipsoid diagrams for the **1.1**, **2.1**, and **3.1** units are shown in Figures 1, S2, and S3, respectively, and the main bond distances and angles are shown in Table S1. It must be noted that the quality of diffraction data corresponding to the Gd^{III} complex (**3**) was not good enough to be fully anisotropically refined. However, these data allow one to unequivocally know not only the raw structure of the complex but also many structural details with a more than enough accuracy to be presented here.

The structure of all of the $\{[\text{M}(\text{3NO}_2, \text{5Br-H}_3\text{L}^{1,1,4})]_2(\mu\text{-F})\}^-$ anions in the unit cells (2 per compound) can be understood as two neutral crystallographically equivalent $[\text{M}(\text{3NO}_2, \text{5Br-H}_3\text{L}^{1,1,4})]$ blocks, joined through a fluoride bridge. Thus, the $[\text{M}(\text{3NO}_2, \text{5Br-H}_3\text{L}^{1,1,4})]$ unit contains the 1,1,4 isomer of the aminophenol donor, which is the same isomer present in the initial mononuclear complex.²⁰ This acts as a trianionic, with all of the phenol oxygen atoms deprotonated and the secondary amine nitrogen atoms protonated. Besides, the ligand behaves as a heptadentate, using all of its oxygen and nitrogen atoms to bind a Ln^{3+} ion. In addition, a fluoride anion bridges the two blocks, thus completing the coordination sphere of the Ln^{3+} centers. This leads to octacoordinated metal ions, with $\text{LnN}_4\text{O}_3\text{F}$ cores. Calculations with the SHAPE program²³ (Table S2) show that the geometry is distorted triangular dodecahedral in all cases. In this polyhedron, the intramolecular $\text{Ln} \cdots \text{Ln}$ distances are ca. 4.5 Å, with a Ln-F-Ln angle of 180° for all of the complexes.

Table 1. Comparison of Some Structural and Magnetic Parameters for Dy^{III} Complexes Magnetostructurally Characterized with Fluoride Ligands

compound ^a	Dy–F distance (Å)	Dy–O distance (Å)	Dy–F–Dy angle (deg)	Dy···Dy _{eq} distance (Å)	c.n./geometry ^b	U _{eff} K (cm ⁻¹)/H _{dc} (Oe)	references
[DyF(oda)(H ₂ O) ₃] _n	2.215(4)/2.249(4)	2.348(4)–2.443(5)	160.26(3)	4.39(7)	8/DD	2.5 (1.7)/0	13
[Dy ₂ F ₂ (oda) ₂ (H ₂ O) ₂] _n	2.245(2)	2.339(3)–2.428(4)	112.39(3)	3.730(4)	8/n.d.	4.9 (3.4)/0	13
[Na ₃ Dy ₂ (valdien) ₂ (μ-F)(μ ⁻ F) ₂ (Cl) ₂ (MeOH) ₂] _n	2.202(3)/2.137(4)/2.209(2)/2.141(4)	2.238(4)–2.278(5)	180.00	4.403(4)/4.418(4)	7/PBPY	49 (34)/0	14
[Dy(Tp ^{py})F(dioxane)](PF ₆)	2.094(4)	2.533(3)			9/JCSAPR	621.6 (432) (FR)	15
[Dy(Tp ^{py})F(pyridine) ₂](PF ₆)	2.0994(16)				9/JCSAPR	759.7 (528) (SR)/0	15
(Bu ₄ N) _{8.5} H _{1.5} [(PW ₁₁ O ₃₉) ₂ Dy ₂ F ₂ (H ₂ O) ₂]	2.325(6)/2.326(6)	2.264(8)–2.366(7)	112.0(3)	3.8549(10)	7/CTPR	483.4 (336)/0	16
[DyLF](CF ₃ SO ₃) ₂	2.123(2)				9/MFF	110 (76.5)/0	17
[C(NH ₃) ₃] ₄ [DyF(piv) ₄](piv) ₂	2.194(2)	2.386(3)–2.557(3)			9/MFF	Raman	18
{[Dy(Tp ^{py})F(L _c)]PF ₆] _n (1c)}	2.098(4)				9/CSAPR	225.9 (157)/0	19
{[Dy(Tp ^{py})F(L _c)]PF ₆] _n (1o)}	2.095(4)				9/CSAPR	225.9 (157)/0	19
Bu ₄ N{[Dy(3-NO ₂ -5-Br-7-H ₃ L ^{1,4})] ₂ (μ-F)} ₂ , 1	2.2764(3)	2.271(3)–2.315(3)	180	4.5528(6)	8/TDD	27.5 (19.1)/600	this work
	2.2717(3)			4.5434(8)			
Bu ₄ N{[Dy(3-Br-5-Cl-H ₃ L ^{1,2,4})] ₂ (μ-F)} ₂ , 4	2.1943(5)	2.237(4)–2.331(4)	169.8(2)	4.3709(8)	8/TDD	25.0 (17.4)/0	this work
						35.9 (24.9)/600	

^aSolvates omitted. oda, oxidiacetate; valdien, dianion of N₁,N₃-bis(3-methoxysalicylidene)diethylenetriamine; Tp^{py}, tris(3-(2-pyridyl)pyrazolyl)pyrazolylhydroborate; L, 1,4,7,10-tetrakis(2-pyridylmethyl)-1,4,7,10-tetraaza-cyclododecane; piv, pivalate. n.d., not described. ^bc.n., coordination number. Geometry: DD, dodecahedron; PBPY, pentagonal bipyramid; JCSAPR, capped square antiprism; MFF, muffin; CTPR, capped trigonal prism; CSAPR, spherical capped square antiprism; TDD, triangular dodecahedron; BTPR, biaugmented trigonal prism; JBTPR, BTPR J50.

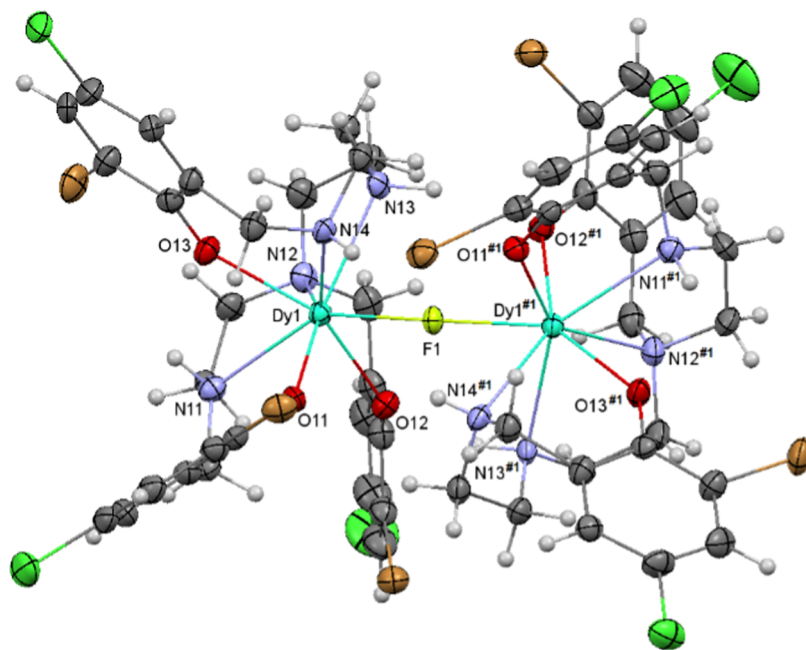


Figure 2. Ellipsoid diagram for the $\{[\text{Dy}(\text{3Br},\text{5Cl}\text{-}\text{H}_3\text{L}^{1,2,4})]_2(\mu\text{-F})\}^-$ anion in 4.

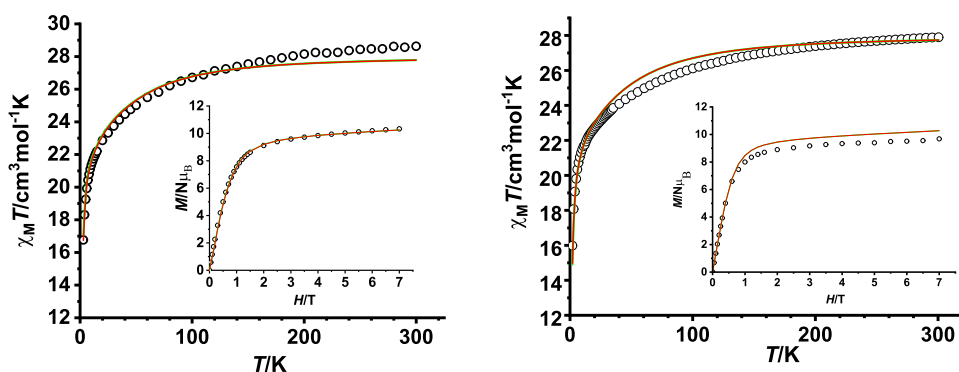


Figure 3. $\chi_M T$ vs T for: (left) 1; (right) 4·2H₂O. Inset: $M/N\mu_B$ vs H at 3 K. The solid lines represent the theoretical data obtained from *ab initio* calculations.

The main Ln–N and Ln–O distances and the angles about the metal centers (Table S1) agree with those expected for complexes with this kind of N,O donor.^{20–22,24} For the Dy^{III} and Gd^{III} compounds, the Ln–F distances are also comparable to the corresponding ones for the scarcely reported single-bridged fluoride dysprosium complexes (Table 1),^{13,14} and, as far as we know, for the only previously crystallographically reported complex with a linear Gd–F–Gd bridge²⁵ within CSD.²⁶ Besides, and as far as one can tell, there is only one previous homonuclear holmium complex with a fluoride bridge crystallographically characterized,²⁷ but, unfortunately, the deposited crystallographic data within CCDC does not allow one to accurately know the geometric parameters (CCDC numbers 115731 and 115732). However, the Ho–F–Ho angle in this polymer is also 180°.

An ellipsoid diagram for $\text{Bu}_4\text{N}\{[\text{Dy}(\text{3Br},\text{5Cl}\text{-}\text{H}_3\text{L}^{1,2,4})]_2(\mu\text{-F})\}\cdot 2\text{H}_2\text{O}\cdot 2\text{THF}$ (4·2H₂O·2THF) is shown in Figure 2, and the main distances and angles are recorded in Table S1. 4·2H₂O·2THF is ionic, as 1·5CH₃C₆H₅-3, and its unit cell contains dinuclear $\{[\text{M}(\text{3Br},\text{5Cl}\text{-}\text{H}_3\text{L}^{1,2,4})]_2(\mu\text{-F})\}^-$ anions and Bu_4N^+ cations, in addition to THF and water as solvates. The anions have an inversion center, which also makes both $[\text{M}(\text{3Br},\text{5Cl}\text{-}$

$\text{H}_3\text{L}^{1,2,4})]$ blocks symmetry-related. In this case, the $[\text{M}(\text{3Br},\text{5Cl}\text{-}\text{H}_3\text{L}^{1,2,4})]$ unit contains a different isomer of the aminophenol donor, the 1,2,4 one, which also acts as a trianionic and heptadentate, with all of the amine nitrogen atoms protonated.

The coordination sphere for the Dy³⁺ center is likewise completed by a fluoride ion, as in 1·5CH₃C₆H₅-3. This also leads to octacoordinated dysprosium atoms, in a N₄O₃F environment.

Calculations of the degree of distortion of this core with the SHAPE program²³ indicate that the geometry around the dysprosium atom is also triangular dodecahedral, but in this case, the polyhedron seems to be more distorted toward a biaugmented trigonal prism than in 1·5CH₃C₆H₅ (Table S2). This highlights the influence of the different isomer of the ligand in the geometry and, hence, in the structural parameters. Accordingly, the Dy–N and Dy–O main distances, and all of the angles about the metal center, agree with those expected for dysprosium complexes with this type of N,O donor,^{20,24} but the DyX–OX1 distances in 4 are significantly shorter than the corresponding ones in 1 (Table S1). In the same way, the Dy–F distance in 4 (*ca.* 2.19 Å) is also within the normal range^{12,13} (Table S1) but notably shorter than in 1 (*ca.* 2.27 Å). Besides,

the DyX–OX1 and DyX–OX2 distances in **1** are on the same order of magnitude as the Dy–F ones, while in **4**, the Dy–F distance is appreciably shorter than the Dy–O ones. The same is true for the intramolecular Dy...Dy distance, considerably shorter in **4** (4.3709(8) Å) than in **1** (ca. 4.55 Å), with a Dy–F–Dy angle more acute than 180° (169.8(2)°, Table S1) in **4**.

Magnetic Properties. Direct-current magnetic susceptibility measurements were recorded for **1**–4·2H₂O as a function of the temperature. The plots of $\chi_M T$ vs T for complexes of the anisotropic Dy^{III} and Ho^{III} ions (**1**, **2**, and 4·2H₂O) are shown in Figures 3 and S4. The $\chi_M T$ values at 300 K are 28.6 cm³ K mol⁻¹ for **1**, 28.5 cm³ K mol⁻¹ for **2**, and 27.9 cm³ K mol⁻¹ for 4·2H₂O, values that are close to the expected ones for two uncoupled Ln³⁺ ions at room temperature (28.34 cm³ K mol⁻¹ for Dy₂ and 28.14 cm³ K mol⁻¹ for Ho₂). In all cases, the $\chi_M T$ product continuously decreases until 2 K. This drop in the curves can be mainly ascribed to thermal depopulation of the excited M_J levels, which leads to the presence of significant single-ion anisotropy, and/or to a weak intramolecular antiferromagnetic coupling between the Ln^{III} ions.

The field dependence of the magnetization at 3 K (Figures 3 and S4) shows that the reduced magnetization at the maximum applied field tends to 10.3 $N\mu_B$ for **1**, 9.4 $N\mu_B$ for **2**, an 9.7 $N\mu_B$ for 4·2H₂O, values that are far away from the theoretically saturated ones anticipated for two isolated Dy^{III} or Ho^{III} ions (of 20 $N\mu_B$ for both ions), thus also suggesting the presence of magnetic anisotropy.

To probe the strength of the magnetic interaction between lanthanoid ions, the synthesis of Gd^{III} analogues is a common practice due to its isotropic nature. Thus, the Gd^{III} complex **3** was successfully synthesized, as previously mentioned, but the gadolinium compound analogous to 4·2H₂O could not be unequivocally characterized. The $\chi_M T$ product for **3** is 16.5 cm³ K mol⁻¹ (Figure 4), a value that is very close to the theoretical

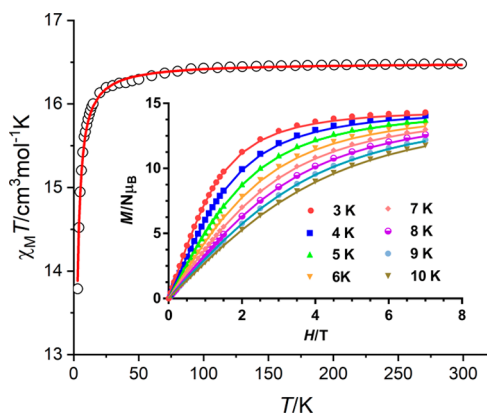


Figure 4. $\chi_M T$ vs T for **3**. Inset: $M/N\mu_B$ vs H at the indicated temperatures. The solid lines correspond to the best fits.

one of 15.76 cm³ K mol⁻¹ for two isolated Gd^{III} ions. This value remains nearly constant until 50 K, and then, it decreases to 13.8 cm³ K mol⁻¹ at 2 K. This decrease could be mainly due to a small intramolecular antiferromagnetic coupling. In this case, the saturated magnetization at 3 K is 14.0 $N\mu_B$, suggesting an $S = 7$ ground state, in agreement with two uncoupled or weakly coupled Gd^{III} ions. The temperature dependence of the $\chi_M T$ product and the field dependence of the magnetization at temperatures between 3 and 10 K were simultaneously fitted to the spin Hamiltonian

$$\hat{H} = -J \vec{s}_1 \vec{s}_2 + g_{\mu_B} \vec{H} \vec{s}$$

with expected values for $S_1 = S_2 = 7/2$ and $\hat{S} = \hat{S}_1 + \hat{S}_2$ using the PHI program.²⁸ In this equation, the first term accounts for the intramolecular coupling and the second one for the Zeeman effect. The best fit yields the parameters $J = -0.062(2)$ cm⁻¹ and $g = 2.047(1)$.

The value of the coupling constant is very small, and it could be considered meaningless. However, it is not possible to reproduce the curves if this intramolecular AF coupling is not considered. Accordingly, these results agree with a weakly coupled antiferromagnetic system, and they are indicative of very weak antiferromagnetic interactions through the Gd–F–Gd bridge. It must be noted that, as far as we know, studies of fluoride-mediated exchange are hitherto unknown in gadolinium chemistry, and this study unequivocally shows that the exchange in linear Gd–F–Gd bridges is very weak and antiferromagnetic in nature. This is a quite expected result, given that it has been well-documented that because of the shielded nature of the 4f orbitals, the coupling between lanthanoid ions is generally small (<0.1 cm⁻¹).^{29,30} The same should also be expected for the coupling constant in **1**, **2**, and 4·2H₂O, in view of the $\chi_M T$ vs T curves, and as the *ab initio* calculations corroborate.

The dynamic magnetic properties for **1**, **2**, and 4·2H₂O were also studied. In a zero dc field, both the in-phase (χ_M' , Figure S5) and out-of-phase (χ_M'' , Figures 5 and S5) signals of the ac

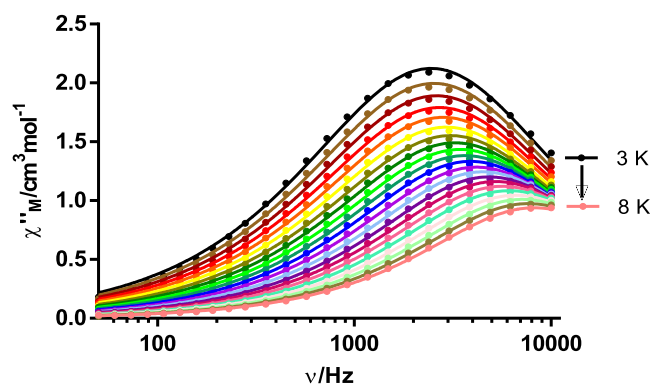


Figure 5. Frequency dependence of χ_M'' for 4·2H₂O in a zero dc field at different temperatures.

susceptibility for 4·2H₂O feature frequency-dependent phenomena, with peaks for χ_M'' in the temperature range 3–8 K. Thus, 4·2H₂O is an SMM. Nevertheless, for **1** and **2**, no peaks for χ_M'' are observed in the absence of a magnetic dc field.

Fitting the Cole–Cole plot to the generalized Debye model for 4·2H₂O yields α parameters in the range of 0.16–0.08, which suggest the presence of more than one relaxation process at low temperatures (Figure S6).

The relaxation time and the energy barrier for 4·2H₂O were extracted from the Arrhenius plot (Figure 6), whose shape also agrees with several relaxation pathways. In this regard, it should be noticed that χ_M'' does not go to zero below the maxima at low temperatures (Figure S5), which indicates a fast relaxation of the magnetization via a QTM mechanism. Consequently, the Arrhenius plot was fitted including not only all of the possible spin-phonon mechanisms but also the QTM relaxation, according to eq 1.

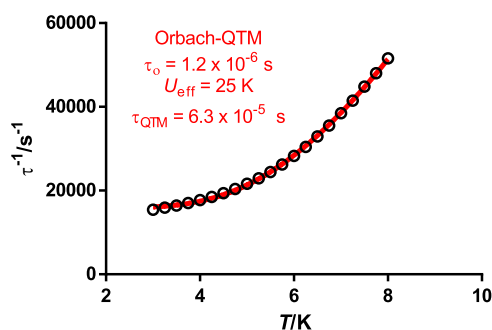


Figure 6. Arrhenius plot for 4·2H₂O in zero field. The red solid line accounts for the best fit considering Orbach plus QTM relaxation processes.

$$\tau^{-1} = \tau_0^{-1} e^{-U_{\text{eff}}/k_B T} + AT + CT^n + \tau_{\text{QTM}}^{-1} \quad (1)$$

However, the direct process (second term of the equation) can already be discarded initially since the ac measurements have been collected in the absence of an external magnetic field. The best fit considering the other three processes, individually or grouped, is achieved with Orbach and QTM relaxation. The introduction of the Raman term, which should dominate the low-temperature relaxation regime,^{31,32} does not improve the fit, and leads to overparameterization. Hence, the best fit yields the parameters $U_{\text{eff}} = 25.0$ K (17.4 cm⁻¹), $\tau_0 = 1.2 \times 10^{-6}$ s, and $\tau_{\text{QTM}} = 6.3 \times 10^{-5}$ s. Accordingly, an appreciable quantum channel is operative in this system. The value of U_{eff} is comparable to that obtained for another dysprosium single-bridged fluoride complex.¹³ Nevertheless, it is worth mentioning that 4·2H₂O is unique among its class (Table 1), given that, as far as we know, it is the first dinuclear dysprosium single fluoride-bridged complex magnetically characterized (Table 1). The other magnetically analyzed Dy^{III} complexes with single μ -F are polymers,^{13,14} and one of them contains diamagnetic metal ions in its unit cell.¹⁴ In addition, a dinuclear dysprosium complex with double fluoride angular bridges has been crystallographically and magnetically studied up to now.¹⁶

Given that the fit of the Arrhenius curve indicates that QTM exists for 4·2H₂O, and that this QTM can also be the cause for the nonobservation of the SMM behavior in **1** and **2**, attempts were made to eliminate this quantum channel. Thus, new ac measurements were recorded under an external dc optimum field of 600 Oe for all of the complexes (Figure S7). Now, χ''_M shows frequency- and temperature-dependent peaks for **1** and 4·2H₂O (Figures 7 and S8), but not for **2**, which does not present slow relaxation of the magnetization even in the presence of an external field. This can be due to the very small energy barrier for the inversion of the spin, or due to the nonelimination of the QTM.

In addition, the χ''_M vs T curves for **1** and 4·2H₂O still do not go to zero at low temperature (Figure S8), indicating that the QTM mechanism has not been fully suppressed by the application of the optimum magnetic field. The fit of the Cole–Cole plots for both complexes yields α parameters in the range of 0.13–0.29 for **1** and 0.31–0.11 for 4·2H₂O (Figure S9). This, along with the nonlinear shape of the Arrhenius plots (Figure 8), indicates the existence of more than one relaxation process in both cases. Accordingly, the Arrhenius plots for **1** and 4·2H₂O were fitted with eq 1, and the best fits taking into account the four processes, individually or grouped, were achieved with only Orbach and QTM relaxation, the latter expected in view of Figure S8. These fits yield the following parameters: $U_{\text{eff}} = 27.5$ K (19.1 cm⁻¹), τ_0

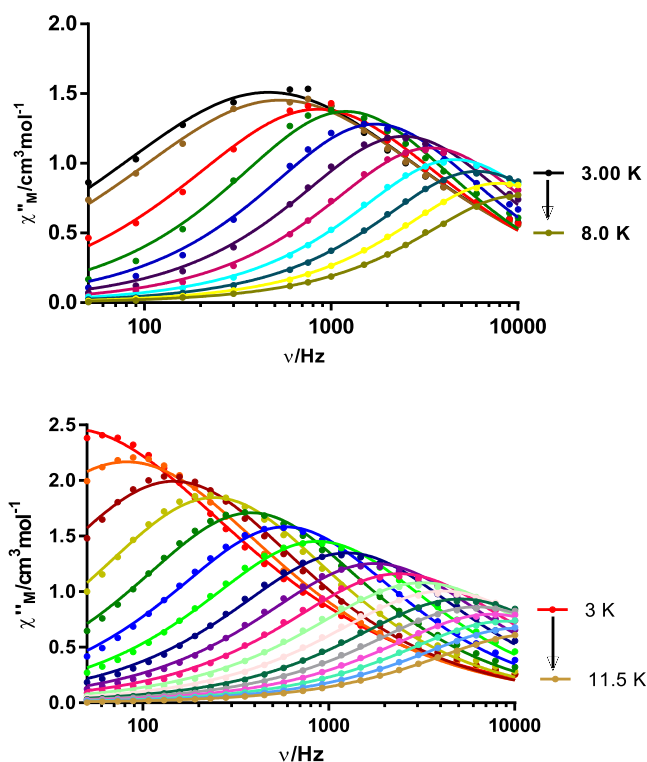


Figure 7. Frequency dependence of χ''_M for **1** (up) and 4·2H₂O (bottom) in $H_{\text{dc}} = 600$ Oe.

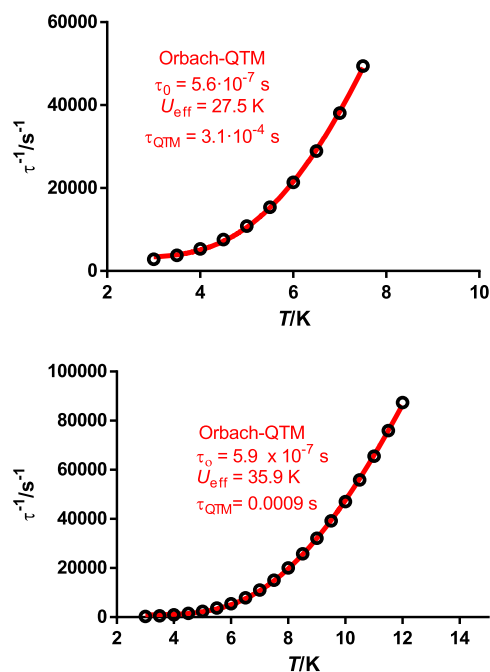


Figure 8. Arrhenius plots for **1** (up) and 4·2H₂O (bottom) in $H_{\text{dc}} = 600$ Oe. The red solid lines account for the best fit considering Orbach and QTM relaxation processes.

$= 5.6 \times 10^{-7}$ s, and $\tau_{\text{QTM}} = 0.0003$ s for **1**, and $U_{\text{eff}} = 35.9$ K (24.9 cm⁻¹), $\tau_0 = 5.9 \times 10^{-7}$ s, and $\tau_{\text{QTM}} = 0.0009$ s for 4·2H₂O. These parameters show that the energy barrier for 4·2H₂O is a bit higher than for **1** in the presence of the magnetic field, but that the observed barrier in both cases is small, and on the same order of magnitude, with a larger quantum tunneling for **1**.

Magneto-Caloric Effect of 3. Polynuclear Gd^{III} complexes can behave as low-temperature molecular magnetic coolers (MMCs) because they show an enhanced magnetocaloric effect (MCE). This effect depends on the change of magnetic entropy after the application of a magnetic field and can potentially be exploited for cooling applications via adiabatic demagnetization.³³ In view of this, we decided to evaluate the magnetothermal properties of 3 because of the following reasons: (i) the antiferromagnetic interaction between the Gd³⁺ ions through the fluoride bridging ligand is very feeble and then appropriate for a large magnetocaloric effect (MCE); (ii) the Gd³⁺ ion is rather isotropic due to the lack of orbital contribution; and (iii) Gd³⁺ has the largest single-ion spin ($S = 7/2$), coming from the 4f⁷ electron configuration.

The magnetic entropy changes ($-\Delta S_m$) that characterize the magnetocaloric properties of 3 can be calculated from the experimental isothermal field-dependent magnetization data (Figure 4) using the Maxwell relation³⁴

$$\Delta S_M = (T, \Delta B) = \int_{H_i}^{H_f} \left[\frac{\partial M(T, B)}{\partial T} \right]_B dH \quad (2)$$

where H_i and H_f are the initial and final applied magnetic fields, respectively. As can be observed in Figure 9, for any applied

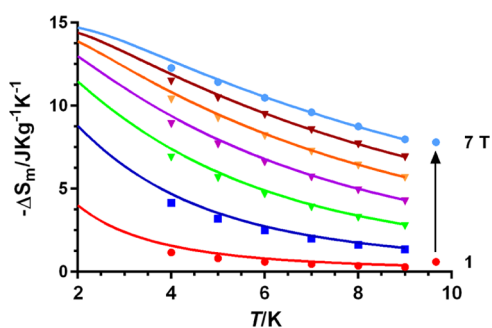


Figure 9. Magnetic entropy changes ($-\Delta S_m$) simulated using $J = -0.062 \text{ cm}^{-1}$ and $g = 2.047$ (solid lines) and calculated from the experimental magnetization data for 3 from 1 to 7 T and temperatures from 4 to 9 K (points).

magnetic field, the values of $-\Delta S_m$ increase with decreasing temperature from 10 to 3 K. The maximum value of $-\Delta S_m$ achieved is $12.27 \text{ J kg}^{-1} \text{ K}^{-1}$ at $T = 4 \text{ K}$, with an applied field change of $\Delta H = 7 \text{ T}$ (Figure 9).

Even though the antiferromagnetic interactions (AF) tend to decrease the values of $-\Delta S_m$ in all cases with regard to the noninteracting systems, when the AF are weak, as in the case of compound 3, multiple close-in-energy low-lying excited and field-accessible states generate, which would permit an easy

polarization of the spin, so that each of these states can contribute to the magnetic entropy of the system, leading to significant $-\Delta S_m$ values at a low magnetic field. We have simulated the MCE for 3 using the magnetic parameters (g and J) extracted from fitting of the isothermal field dependence of the magnetization and susceptibility data (Figure 9). The simulated $-\Delta S_m$ values are almost equal to those extracted from the Maxwell equations (Figure 9), thus supporting the $-\Delta S_m$ values, and also the coupling constant J , extracted from experimental magnetic measurements.

The simulated MCE value at 2 K and 7 T ($14.70 \text{ J kg}^{-1} \text{ K}^{-1}$) is only somewhat lower than that calculated for the full magnetic entropy content per mole $nR \ln(2s_{\text{Gd}} + 1) = 4.16$, $R = 15.41 \text{ J kg}^{-1} \text{ K}^{-1}$ for 3. Moreover, the extracted $-\Delta S_m$ values are found in the low limit of the MCE observed for other Gd₂ complexes,^{33c} which can mainly be attributed to the low magnetic density of 3 ($n^\circ \text{ Gd}^{3+}/\text{MW}$), because the increase in magnetic density produces an increase of MCE. This result again highlights the essential role of magnetic density on the magnitude of the MCE.

Ab Initio Calculations. To gain more insights into the magnetic properties of the studied compounds, *ab initio* calculations were performed for dysprosium and the holmium complexes based on their single-crystal X-ray structures (see Computational Details) without solvates. This decision was based on our own experience, which shows that solvates do not have a significant influence on the calculations in this kind of complex.^{8,20,24c} In addition, for 1 and 2, calculations were performed for the crystallographically different X.1 and X.2 ($X = 1$ or 2) complexes present in the unit cell. Fragment calculations were made for both halves, but due to symmetry reasons, only the results of one Ln for each complex are shown and have been discussed (see Tables S3–S5).

The obtained g -factors for 1 and 4 are collected in Table 2. Both complexes show a large axial character of the ground state but with nonzero g_x and g_y components, indicating a relatively non-negligible QTM, as is experimentally observed.

The direction of the easy axis will depend on the coordinated ligands. For the Dy^{III} compounds, the oblate shape of the electron density of the Dy^{III} center will be accommodated between the ligands surrounding the metal in the best possible way to reduce the electronic repulsion. The coordinated ligands have three monoanionic phenolic oxygen atoms (OX1, OX2, and OX3 in both compounds), and the Dy^{III} centers are bridged by the fluoride anion. Three of those negatively charged donors (two phenolic oxygen atoms, OX1 and OX3, and the fluoride) are in the same plane, and the oblate electron density of the Dy^{III} center will avoid that plane from being perpendicular to it. Consequently, the directions of the g_z component will be in that plane in both compounds. In both cases, there is a phenolic

Table 2. Calculated g Components for 1.1, 1.2, and 4 for the Ground and First Excited States at the CASSCF Level^a

compound	1.1		1.2		4	
	GS	1st ES	GS	1st ES	GS	1st ES
g_x	0.137	0.802	0.111	1.134	0.050	0.285
g_y	0.314	6.207	0.269	2.041	0.140	0.518
g_z	19.097	10.942	19.222	15.470	18.909	14.842
θ (deg)	58.0		59.1		28.1	
γ (deg)	139.8		34.4		2.5	

^a θ , angle between the g_z vector and the vector connecting both Dy^{III} in the dinuclear molecule; γ , angle between the g_z vectors of the ground and first excited states.

oxygen atom close to the fluoride (OX1, O–Dy–F angle of about 74°) and another further away (OX3, O–Dy–F angle of about 142°). To minimize repulsions, the oblate electron density of the Dy^{III} center will be allocated between the phenolic oxygen OX1 and fluoride atoms, and the second phenolic oxygen, OX3. In the case of **4**, the Dy–F distance is the shortest one, and the g_z component is located closer to the fluoride, while in **1**, the distances Dy–O and Dy–F are very similar, as previously discussed, and the g_z component is located closer to the phenolic oxygen OX1 (see Figure 10). As a result, the angle between the g_z vector and the vector connecting both Dy^{III} ions (θ) in the dinuclear molecule is quite different (see Table 2), which will affect the dipolar exchange coupling, *vide infra*.

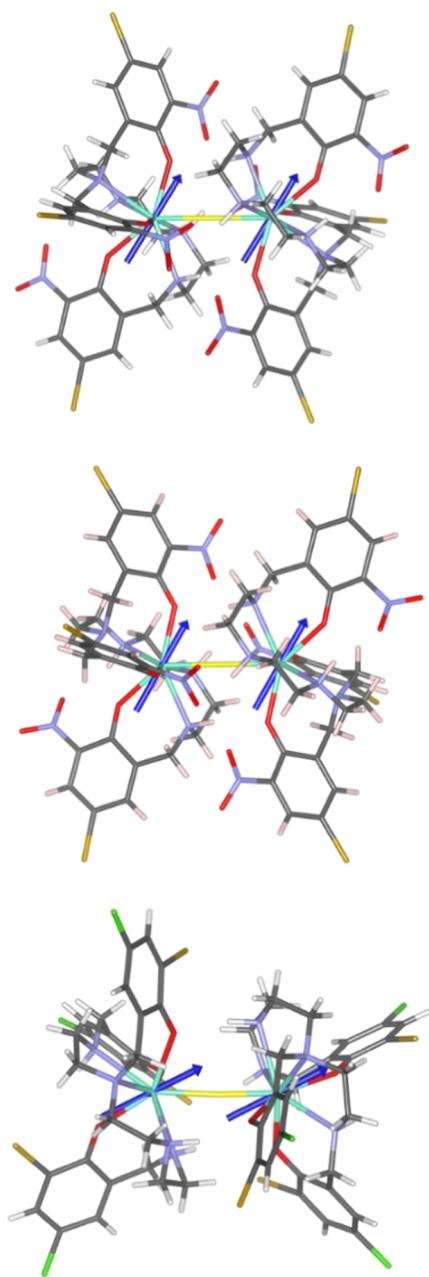


Figure 10. Molecular structures of **1.1** (up), **1.2** (middle), and **4** (bottom) showing the g_z calculated directions of the g components of the Dy^{III} centers in the ground state.

The analysis of the lowest energy states before inclusion of the spin–orbit effect, collected in Table S3, shows that the first excited state is very close in energy in all of the cases (between 14 and 20.6 cm^{-1}), while the second excited state is further away (between 106.3 and 146 cm^{-1}). Some of us previously noticed that the value of $(E_2 - E_1)/E_1$ is a figure of merit of the axiality in mononuclear Dy compounds.³⁵ Herein, the ratio is larger in compound **4**. This usually results in a large axiality because the two states that are very close in energy, the ground and first excited states, are very axial, while the second excited state has a less axial character. However, as can be observed in the g_i components of the g factor in Table 2, here, the ground state is quite axial in both **1** and **4** (although in **4** the g_x and g_y components are smaller), but the excited states for **4** are more axial than for **1**. Nevertheless, the analysis of the energies of the lowest KDs after the inclusion of the SOC states shows a large energy difference between the ground and the first excited KDs (around 100 cm^{-1}) in all of the cases (Table S4), although the next KD (the second excited state) is very close in energy to the first state for compound **1.1**.

When looking at the transition probabilities between the states of the individual fragments (Figure 11), it can also be seen that in all of the complexes the quantum tunnel probability in the ground state is lower than 0.1, and that the probabilities are in general smaller for **4** than for **1**, which is in concordance with the small values of g_x and g_y in Table 2. In the case of compound **4**, the Orbach relaxation through the first excited state has a probability lower than 0.1, which is in concordance also with the close-to-parallel orientation of the easy axis in both the ground and first excited states (see Table 2). Thus, the expected mechanism would be thermally assisted QTM through the first KD (U_{eff} ca. 100 cm^{-1}), but the Orbach process through the second excited state is also highly probable (U_{eff} ca. 156 cm^{-1}), especially if an external field is applied.

For **1**, the predominant mechanism seems to be Orbach relaxation through the first excited state in both cases, with an energy of ca. $96\text{--}102\text{ cm}^{-1}$. Besides, although the mechanism seems to be the same in **1.1** and **1.2**, several differences can be observed. For **1.1** the second excited state is closer in energy to the first one, and it has a larger tunneling probability in the first excited state than that observed for **1.2**, which might be related to the larger axiality of the first excited state in **1.2** (Table 2). The obtained values, although quite far from the calculated ones from magnetic measurements, allow explaining the experimental results. Accordingly, **1** is not an SMM, and this can be related to the more feasible QTM mechanism for **1** compared to **4**. This agrees with the fact that slow relaxation of the magnetization appears experimentally for **1** only in the presence of a magnetic field, thus revealing the strong QTM for **1**. The best magnetic behavior of **4**, which is an SMM, compared to **1**, is also justified by the *ab initio* calculations, given that they clearly demonstrate that the ground state and, specially, the first excited state are more axial (smaller g_x and g_y values) in **4** than in **1** and that the QTM is less probable in **4**.

Nevertheless, the experimentally calculated U_{eff} value for **4** (24.9 cm^{-1} in $H_{\text{dc}} = 600\text{ Oe}$) differs significantly from the theoretical one. The same occurs for **1** (19.1 cm^{-1} in $H_{\text{dc}} = 600\text{ Oe}$). This difference could perhaps be ascribed to some effects related to magnetic interactions, which possibly are not considered in the *ab initio* calculations, and also to the presence of other competing relaxation mechanisms. In spite of this, these studies show the same experimental trend, and are in agreement with the fact that the compound with the 3Br,3Cl substituents

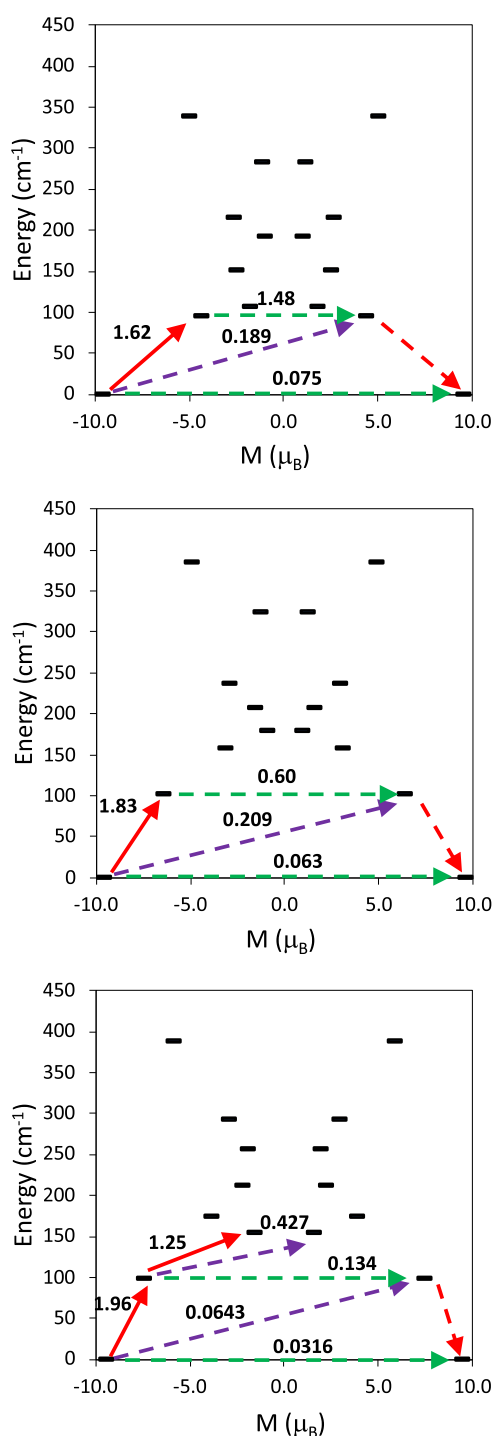


Figure 11. States' energies as a function of their average magnetic moment, M , along the main anisotropy axis for the individual fragments of compounds **1.1** (top), **1.2** (middle), and **4** (bottom). The dashed green arrows correspond to the quantum tunneling mechanism of the ground or excited states, and the dashed purple arrow shows the hypothetical Orbach relaxation process. The solid red arrow indicates the transition between the ground and excited Kramers doublets, and the dashed red arrow indicates the excitation pathway to the ground state with the reversed spin. The values close to the arrows indicate the matrix elements of the transition magnetic moments (above 0.1, an efficient spin relaxation mechanism is expected).

has better magnetic properties than the compound with the $3\text{NO}_2, 5\text{Br}$ substituents, as we have already published.²⁰

However, in this case, the difference in the magnetic behavior seems not to be attributable to the greater electrophilic character of the substituents in **1**, but rather seems to be related to structural changes resulting from the presence of the 1,1,2 isomer of the ligand in **1** and the 1,2,4 one in **4**.

The magnetic coupling interaction between Dy^{III} centers in both complexes has been also studied by means of POLY_ANISO software and the implemented Lines model. Both magnetization and susceptibility curves were fitted simultaneously with and without the inclusion of the dipolar magnetic coupling, and we found a reasonable agreement with the experimental susceptibility and magnetization curves (Figure 3). For compound **4**, if the magnetic dipolar coupling is not included, the obtained coupling constant is -0.14 cm^{-1} , while if we include the dipolar coupling, then the coupling constant value is -0.29 cm^{-1} , showing the ferromagnetic nature of the dipolar coupling ($+0.15 \text{ cm}^{-1}$). In the case of **1**, however, the coupling is smaller, and it goes from -0.10 (-0.106) cm^{-1} to -0.094 (-0.094) cm^{-1} for **1.1** (**1.2**) when the dipolar coupling is considered. In this case, this dipolar coupling is antiferromagnetic and very small (*ca.* -0.01 cm^{-1}). The magnetic dipolar coupling mainly depends on the magnetic moments of the interacting centers, their relative orientation, and the distance between them. Their expression can be simplified into eq 3 in the case of two parallel interacting magnetic moments, which is the case in both dysprosium compounds.

$$E_{\text{dip}} = -\left[\frac{\mu_0}{4\pi}\right] \frac{\mu_i \mu_j}{r^3} [3 \cos^2(\theta) - 1] \quad (3)$$

In eq 3, it can be seen how it depends on the angle between the magnetic moment and the vector connecting both magnetic centers. When this angle is smaller than 54.75° , the coupling is ferromagnetic, while when it is larger, it is antiferromagnetic. In addition, the coupling is maximized when the magnetic moment and the vector connecting both magnetic centers are parallel or perpendicular. As can be seen in Figure 10 and Table 2, for compound **4**, the angle is smaller (*ca.* 28°) and for **1** it is slightly larger (*ca.* 58 – 59°) than 54.75° , which agrees with the obtained ferromagnetic dipolar coupling for **4**, and the very small and antiferromagnetic coupling for **1**. Additionally, the exchange coupling through the fluoride bridge is relatively weak and antiferromagnetic in both cases, -0.094 cm^{-1} for **1** and -0.29 cm^{-1} for **4**. The weak exchange coupling is expected for lanthanoid ions, although herein, larger coupling is observed for Dy in comparison to Gd ions, especially in compound **4**, which might be related to the differences in the bridge. Due to the small value of the exchange interaction, the consideration of the exchange/dipolar interaction on the low-lying spectrum gives rise to a similar energy barrier (Tables S6–S8). In the low-lying spectrum, there are four states very low in energy (less than 2 K) due to the possible ferro- and antiferromagnetically coupling states of the ground KDs, which will be populated at the temperature of the experiment. At an energy closer to the first excited KD in the individual fragments, eight states would be found resulting from the coupling of the ground KDs and the first excited KDs. The transition probabilities also found in this scheme show that the relaxation will be through states at the same energy differences as those found for the individual fragments.

Accordingly, these results clearly show that small structural changes can lead to very significant changes in the dipolar interactions and, hence, in the magnetic behavior of metal

complexes although the calculated energy barriers in these cases are not affected.

In the case of compound **2**, the lowest energy states can be described as 5I_8 ground multiplets of the Ho^{III} center, which are split in a range of 250 cm^{-1} (Table S5), which is similar to other Ho compounds.^{24c,36} The small energy difference between the ground state and the first excited states may account for the absence of slow relaxation even in the presence of an external field, to which the large QTM in this non-Kramer system can also contribute. The magnetic coupling interaction between Ho^{III} centers has been also studied with the same procedure employed for the Dy analogue (**1**). In this case, although the calculations reproduce the curve worse than for the dysprosium compounds, and there are several fitting possibilities, the experimental values can be reasonably simulated with a small J value of -0.1 cm^{-1} (Figure S4), similar to that of compound **1**.

In addition, DFT calculations for the gadolinium complex **3**, based on its single-crystal X-ray structure, were also performed (see the Computational Details). The calculated J value for this dinuclear Gd_2 complex ($\hat{H} = -J\hat{S}_1\hat{S}_2$) is -0.028 cm^{-1} . Despite the tiny value, it is on the same order of magnitude as the experimental one (-0.062 cm^{-1}), and the antiferromagnetic character is well reproduced. This calculated value corresponds to the exchange term, and experimentally, such a contribution is also mixed with dipolar interactions, which are expected to be smaller. Thus, these calculations also validate the experimental small antiferromagnetic exchange mediated by the linear fluoride bridge in the gadolinium complex **3**.

CONCLUSIONS

This work describes a new synthetic method for isolating linear fluoride single-bridged dinuclear complexes from mono-aquo mononuclear precursors. All of the four complexes described herein contribute to an increase in the scarce number of fluoride-lanthanoid coordination compounds crystallographically and magnetically studied. Thus, the Gd^{III} complex **3** is, as far as we know, the first crystallographically and magnetically analyzed gadolinium complex with a fluoride bridge. The magnetic study shows that the coupling constant through a linear $\text{Gd}-\text{F}-\text{Gd}$ bridge is small and antiferromagnetic in nature, and this was also sustained by theoretical calculations. **2** is the first fluoride holmium complex to be magnetically analyzed and, to the best of our knowledge, the second one of being crystallographically characterized. Nevertheless, **2** does not show slow relaxation of the magnetization even in the presence of a magnetic field, while dysprosium complexes **1** and $4\cdot 2\text{H}_2\text{O}$ do. However, while $4\cdot 2\text{H}_2\text{O}$ is an SMM, **1** only presents an SMM-like behavior under a magnetic field of 600 Oe. The U_{eff} barriers for **1** and $4\cdot 2\text{H}_2\text{O}$ are on the same order of magnitude, being a bit smaller for **1** than for $4\cdot 2\text{H}_2\text{O}$. This tendency is also corroborated by *ab initio* studies, which show the less axial character, and the most probable QTM for **1**, as well as justify the absence of SMM behavior for **2**. These calculations also highlight the different dipolar interactions in **1** (antiferromagnetic) and $4\cdot 2\text{H}_2\text{O}$ (ferromagnetic), and further support the overall antiferromagnetic nature of the coupling constant in **3**.

EXPERIMENTAL SECTION

Materials and General Methods. All chemical reagents were purchased from commercial sources and used as received without further purification. Elemental analyses of C, H, and N were performed on a ThermoScientific Flash Smart analyzer. The ligands were prepared as previously reported.²⁰

Synthesis of the Complexes. Mononuclear Complexes. The mononuclear precursors $[\text{Dy}(\text{3Br}_5\text{Cl-H}_3\text{L}^{1,1,4})(\text{H}_2\text{O})]\cdot 0.25\text{MeOH}$ and $[\text{Dy}(\text{3NO}_2\text{5Br-H}_3\text{L}^{1,1,4})(\text{H}_2\text{O})]$ were obtained as previously reported by us,²⁰ while $[\text{Ho}(\text{3NO}_2\text{5Br-H}_3\text{L}^{1,1,4})(\text{H}_2\text{O})]$ and $[\text{Gd}(\text{3NO}_2\text{5Br-H}_3\text{L}^{1,1,4})(\text{H}_2\text{O})]$ are new, and were prepared in a similar way, exemplified by the isolation of $[\text{Ho}(\text{3NO}_2\text{5Br-H}_3\text{L}^{1,1,4})(\text{H}_2\text{O})]$: To a solution of $3\text{NO}_2\text{5Br-H}_3\text{L}^{1,1,4}$ (0.100 g, 0.120 mmol) in acetonitrile/chloroform (20/15 mL), triethylamine (0.036 g, 0.359 mmol) is added. Then, a solution of holmium nitrate pentahydrate (0.053 g, 0.120 mmol) in acetonitrile (15 mL) is added to the ligand solution, and the mixture is stirred at room temperature for 24 h. The solution is filtered to avoid any possible impurity, and then, it is concentrated in a rotaevaporator up to 15 mL. The precipitated solid is filtered and dried in an oven for 4 h. Yield: 0.056 g (47%). M.W.: 1013.14 g/mol. Anal. calcd for $\text{C}_{27}\text{H}_{26}\text{Br}_3\text{HoN}_7\text{O}_{10}$ (%): C 32.01, N 9.68, H 2.59. Found: C 32.59, N 9.85, H 2.43.

$[\text{Gd}(\text{3NO}_2\text{5Br-H}_3\text{L}^{1,1,4})(\text{H}_2\text{O})]$. $3\text{NO}_2\text{5Br-H}_3\text{L}^{1,1,4}$ (0.200 g, 0.240 mmol) in methanol (10 mL)/chloroform (10 mL), NaOH solution (0.029 g, 0.717 mmol) in methanol (5 mL); $\text{Gd}(\text{NO}_3)_3\cdot 6\text{H}_2\text{O}$ (0.108 g, 0.239 mmol) in methanol (5 mL). Yield: 0.163 g (68%). M.W.: 1008.52 g/mol. Anal. calcd for $\text{C}_{27}\text{H}_{26}\text{Br}_3\text{GdN}_7\text{O}_{10}$: C 32.15, N 9.72, H 2.90. Found: C 31.99, N 9.75, H 3.00.

Fluoride-Bridged Complexes. All of the dinuclear fluoride-bridged complexes were obtained in a similar way, from the mononuclear complexes $[\text{Dy}(\text{3NO}_2\text{5Br-H}_3\text{L}^{1,1,4})(\text{H}_2\text{O})]$, $[\text{Ho}(\text{3NO}_2\text{5Br-H}_3\text{L}^{1,1,4})(\text{H}_2\text{O})]$, $[\text{Gd}(\text{3NO}_2\text{5Br-H}_3\text{L}^{1,1,4})(\text{H}_2\text{O})]$, and $[\text{Dy}(\text{3Br}_5\text{Cl-H}_3\text{L}^{1,1,4})(\text{H}_2\text{O})]\cdot 0.25\text{MeOH}$. Their isolation is exemplified by the synthesis of $\text{Bu}_4\text{N}\{[\text{Dy}(\text{3NO}_2\text{5Br-H}_3\text{L}^{1,1,4})_2(\mu\text{-F})]\}$ (**1**): To a MeOH/THF (25/25 mL) solution of $[\text{Dy}(\text{3NO}_2\text{5Br-H}_3\text{L}^{1,1,4})(\text{H}_2\text{O})]$ (0.086 g, 0.085 mmol), Bu_4NF (0.027 g, 0.085 mmol) is added. The mixture is stirred overnight, and a solution is obtained. The solution is filtered to eliminate any impurity and left to slowly evaporate. After 2 days, an orange powder precipitates, which is isolated by filtration. Recrystallization of the orange powder in toluene gives rise to single crystals of $1\cdot 5\text{CH}_3\text{C}_6\text{H}_5$. The crystals lose the toluene solvate on drying. Yield: 0.072 g (38%). M.W.: 2252.98 g/mol. Anal. calcd for $\text{C}_{70}\text{H}_{90}\text{Br}_6\text{Dy}_2\text{N}_{15}\text{O}_{18}\text{F}$: C 37.32, N 9.33, H 4.03%. Found: C 37.15, N 9.18, H 4.08.

$\text{Bu}_4\text{N}\{[\text{Ho}(\text{3NO}_2\text{5Br-H}_3\text{L}^{1,1,4})_2(\mu\text{-F})]\}$ (**2**). $[\text{Ho}(\text{3NO}_2\text{5Br-H}_3\text{L}^{1,1,4})(\text{H}_2\text{O})]$ (0.174 g, 0.171 mmol) in THF (25 mL); Bu_4NF (0.055 g, 0.171 mmol). Slow evaporation of the obtained solution yields single crystals of the $2\cdot 2\text{H}_2\text{O}\cdot 0.75\text{THF}$, suitable for single X-ray diffraction studies. The crystals lose the solvates on drying, to produce **2**. Yield: 0.123 g (32%). M.W.: 2257.84 g/mol. Anal. Calcd for $\text{C}_{70}\text{H}_{90}\text{Br}_6\text{Ho}_2\text{N}_{15}\text{O}_{18}\text{F}$: C 37.24, N 9.31, H 4.02%. Found: C 37.10, N 9.42, H 4.33%.

$\text{Bu}_4\text{N}\{[\text{Gd}(\text{3NO}_2\text{5Br-H}_3\text{L}^{1,1,4})_2(\mu\text{-F})]\}$ (**3**). $[\text{Gd}(\text{3NO}_2\text{5Br-H}_3\text{L}^{1,1,4})(\text{H}_2\text{O})]$ (0.193 g, 0.191 mmol) in MeOH/THF (25/25 mL) THF (25 mL). Bu_4NF (0.051 g, 0.191 mmol). Single crystals of **3**, suitable for single X-ray diffraction studies, are obtained from the mother liquors. Yield: 0.160 g (37%). M.W.: 2242.48 g/mol. Anal. calcd for $\text{C}_{70}\text{H}_{90}\text{Br}_6\text{Gd}_2\text{N}_{15}\text{O}_{18}\text{F}$: C 37.49, N 9.37, H 4.05%. Found: C 37.02, N 9.17, H 4.01%.

$\text{Bu}_4\text{N}\{[\text{Dy}(\text{3Br}_5\text{Cl-H}_3\text{L}^{1,2,4})_2(\mu\text{-F})]\cdot 2\text{H}_2\text{O}$ (**4**) $\cdot 2\text{H}_2\text{O}$). $[\text{Dy}(\text{3Br}_5\text{Cl-H}_3\text{L}^{1,1,4})(\text{H}_2\text{O})]\cdot 0.25\text{MeOH}$ (0.148 g, 0.149 mmol), Bu_4NF (0.039 g, 0.149 mmol) in MeOH/THF (25/25 mL). Slow evaporation of the obtained solution directly renders single crystals of $4\cdot 2\text{H}_2\text{O}\cdot 2\text{THF}$, suitable for X-ray diffraction studies, which loses the THF solvate to give rise to $4\cdot 2\text{H}_2\text{O}$. Yield: 0.116 g (35%). M.W.: 2225.60. Anal. calcd for $\text{C}_{70}\text{H}_{94}\text{Dy}_2\text{Br}_6\text{Cl}_6\text{N}_9\text{O}_8$: C 37.77, N 5.66, H 4.26%. Found: C 37.51, N 5.53, H 4.09%.

Single X-ray Diffraction Studies. Crystal data and details of refinement are given in Table S9. The single crystals of $1\cdot 5\text{CH}_3\text{C}_6\text{H}_5$, $2\cdot 2\text{H}_2\text{O}\cdot 0.75\text{THF}$, **3**, and $4\cdot 2\text{H}_2\text{O}\cdot 2\text{THF}$ could be obtained as detailed above. Data were collected at 100 K on a Bruker D8 VENTURE PHOTON III-14 diffractometer, employing graphite monochromatized Mo-K α ($\lambda = 0.71073 \text{ \AA}$) radiation. Multiscan absorption corrections were applied using the SADABS routine.³⁷ The structures were solved by standard direct methods employing SHELXT³⁸ and then refined by full matrix least-squares techniques on F^2 using SHELXL, from the program package SHELX-2018.³⁸ As a general

method, all atoms different from hydrogen were anisotropically refined, while H atoms were typically included in the structure factor calculations in geometrically idealized positions. However, with the intention of revealing the hydrogen bonding scheme, hydrogen atoms attached to amine nitrogen atoms were located in the corresponding Fourier map. In this case, either they were freely refined or their thermal parameters were derived from their parent atoms.

As commented in the text, it must be noted that the quality of data corresponding to the gadolinium complex **3** was not good enough to be so fully refined as would be desirable. Thus, basically, only atoms different from C and H were anisotropically refined. Despite the remaining electron densities being higher than usual, it must be commented that an attempt to apply SQUEEZE to avoid unassigned electron densities in voids proved useless. Likewise, most of the unassigned charge was found close to the gadolinium and bromine ions. This indicates that significant molecules were not omitted in this crystal structure.

Powder X-ray Diffraction Studies. The powder diffractograms for $1-4\cdot 2\text{H}_2\text{O}$ were recorded on a Philips diffractometer with a control unity type "PW1710", a vertical goniometer type "PW1820/00", and a generator type "Enraf Nonius FR590", operating at 40 kV and 30 mA, using monochromated $\text{Cu K}\alpha$ ($\lambda = 1.5418 \text{ \AA}$) radiation. A scan was performed in the range $2 < 2\theta < 50^\circ$ with $t = 3 \text{ s}$ and $\Delta 2\theta = 0.02^\circ$. LeBail refinement was obtained with the aid of HighScore Plus Version 3.0d.

Magnetic Measurements. Magnetic susceptibility dc and ac measurements for microcrystalline samples of $1-4\cdot 2\text{H}_2\text{O}$ were carried out with a PPMS Quantum Design susceptometer. The dc magnetic susceptibility data were recorded under a magnetic field of 1000 Oe in the range of 2–300 K. Magnetization measurements at different temperatures (ranging from 2.0 to 7.0 K) were recorded under magnetic fields ranging from 0 to 70 000 Oe. Diamagnetic corrections were estimated from Pascal's Tables. Alternating current (ac) susceptibility measurements for **1**, **2**, and $4\cdot 2\text{H}_2\text{O}$ were performed at zero dc field and at 600 Oe dc field, with an oscillating ac field of 3.5 Oe and ac frequencies ranging from 50 to 10 000 Hz.

Computational Details. Orca software (version 5.0.3) was employed to perform multireference calculations³⁹ based on the single-crystal X-ray structures of complexes $1\cdot 5\text{CH}_3\text{C}_6\text{H}_5$, $2\cdot 2\text{H}_2\text{O}\cdot 0.75\text{THF}$, and $4\cdot 2\text{H}_2\text{O}\cdot 2\text{THF}$. The fragment approach, where one of the metals is substituted by the close shell La^{3+} ion, was employed to study independently each metal in each dinuclear compound. Due to the symmetry of the molecule, only the results for one of the metals is shown because they were identical.

Due to the large ionic character of the Ln–O/N/F bonds, the inclusion of the dynamic correlation contributions is not necessary. The def2-TZVP basis set was used.^{40,41} For the Dy, a (9,7) active space was employed and 21 sextets, 128 quadruplets, and 98 doublets were considered. In the case of Ho, a (10,7) active space was considered and 35 sextets, 210 quadruplets, and 196 doublets were included. The Single_Aniso and Poly_Aniso⁴² stand-alone utilities, distributed with Orca 5.0.3, were employed to evaluate the magnetic properties of the individual fragments and the simulation of the anisotropic exchange interactions. The energy barrier was evaluated with the probability of transition between two different states of the molecules using the matrix elements of the transition magnetic moments, which have been calculated as proposed by the golden Fermi rule, as the integral between the two involved states using a magnetic moment operator.⁴³

For the calculation of the exchange coupling constant of complex **3**, DFT calculations were performed with the all-electron FHI-aims computer code using a numerical local orbital basis set (tight basis set in such a computer code).⁴⁴ This approach allows for full-potential calculations at a low computational cost without using any a priori approximations for the potential, such as pseudopotentials or frozen cores. The calculations were performed using the single-crystal X-ray structures of **3** and the hybrid B3LYP exchange–correlation functional.⁴⁵ The calculation of the J coupling was performed using the nonprojected option.⁴⁶

■ ASSOCIATED CONTENT

SI Supporting Information

The Supporting Information is available free of charge at <https://pubs.acs.org/doi/10.1021/acs.inorgchem.2c00773>.

Figures S1–S9 and Tables S1–S9 (PDF)

Accession Codes

CCDC 2127468–2127471 contain the supplementary crystallographic data for this paper. These data can be obtained free of charge via www.ccdc.cam.ac.uk/data_request/cif, or by emailing data_request@ccdc.cam.ac.uk, or by contacting The Cambridge Crystallographic Data Centre, 12 Union Road, Cambridge CB2 1EZ, UK; fax: +44 1223 336033.

■ AUTHOR INFORMATION

Corresponding Author

Matilde Fondo – Departamento de Química Inorgánica, Facultad de Química, Universidad de Santiago de Compostela, 15782 Santiago de Compostela, Spain; orcid.org/0000-0002-7535-946X; Email: matilde.fondo@usc.es

Authors

Julio Corredoira-Vázquez – Departamento de Química Inorgánica, Facultad de Química, Universidad de Santiago de Compostela, 15782 Santiago de Compostela, Spain; orcid.org/0000-0002-7806-179X

Cristina González-Barreira – Departamento de Química Inorgánica, Facultad de Química, Universidad de Santiago de Compostela, 15782 Santiago de Compostela, Spain; orcid.org/0000-0001-9975-597X

Ana M. García-Deibe – Departamento de Química Inorgánica, Facultad de Química, Universidad de Santiago de Compostela, 15782 Santiago de Compostela, Spain; orcid.org/0000-0001-9127-0740

Jesús Sanmartín-Matalobos – Departamento de Química Inorgánica, Facultad de Química, Universidad de Santiago de Compostela, 15782 Santiago de Compostela, Spain; orcid.org/0000-0002-9971-4657

Silvia Gómez-Coca – Departament de Química Inorgànica i Orgànica, and Institut de Química Teòrica i Computacional, Universitat de Barcelona, 08028 Barcelona, Spain; orcid.org/0000-0002-2299-4697

Eliseo Ruiz – Departament de Química Inorgànica i Orgànica, and Institut de Química Teòrica i Computacional, Universitat de Barcelona, 08028 Barcelona, Spain; orcid.org/0000-0001-9097-8499

Enrique Colacio – Departamento de Química Inorgánica, Facultad de Ciencias, Universidad de Granada, 18071 Granada, Spain

Complete contact information is available at: <https://pubs.acs.org/doi/10.1021/acs.inorgchem.2c00773>

Author Contributions

The manuscript was written through contributions of all authors. All authors have given approval to the final version of the manuscript.

Notes

The authors declare no competing financial interest.

ACKNOWLEDGMENTS

The authors thank the Spanish Ministerio de Ciencia e Innovación projects (PGC2018-102052-B-C21, PGC2018-093863-B-C21, MCIN/AEI/10.13039/501100011033/FEDER “Una manera de hacer Europa”) for financial support. E.C. acknowledges Junta de Andalucía for the FEDER Andalucía project A-FQM-172-UGR18. J.C.-V. also thanks Xunta de Galicia for his Ph.D. fellowship (ED481A-2018/136). The authors acknowledge computer resources, technical expertise, and assistance provided by the CSUC.

REFERENCES

- (1) Rinehart, J. D.; Long, J. R. Exploiting single-ion anisotropy in the design of f-element single-molecule magnets. *Chem. Sci.* **2011**, *2*, 2078–2085.
- (2) Guo, F.-S.; Day, B. M.; Chen, Y.-C.; Tong, M.-L.; Mansikkam-ki, A.; Layfield, R. A. Magnetic hysteresis up to 80 kelvin in a dysprosium metallocene single-molecule magnet. *Science* **2018**, *362*, 1400–1403.
- (3) Gould, C. A.; McClain, K. R.; Reta, D.; Kragoskow, J. G. C.; Marchiori, D. A.; Lachman, E.; Choi, E.-S.; Analytis, J. G.; Britt, R. D.; Chilton, N. F.; Harvey, B. G.; Long, J. R. Ultrahard magnetism from mixed-valence dlanthanide complexes with metal-metal bonding. *Science* **2022**, *375*, 198–202.
- (4) Zhu, L.; Dong, Y.; Yin, B.; Ma, P.; Li, D. Improving the single-molecule magnet properties of two pentagonal bipyramidal Dy³⁺ compounds by the introduction of both electron-withdrawing and -donating groups. *Dalton Trans.* **2021**, *50*, 12607–12618.
- (5) Moilanen, J. O.; Mansikkamäki, A.; Lahtinen, M.; Guo, F.-S.; Kalenius, E.; Layfield, R. A.; Chibotaru, L. F. Thermal expansion and magnetic properties of benzoquinone-bridged dinuclear rare-earth complexes. *Dalton Trans.* **2017**, *46*, 13582–13589.
- (6) Liu, J.-L.; Chen, Y.-C.; Tong, M.-L. Symmetry strategies for high performance lanthanide-based single-molecule magnets. *Chem. Soc. Rev.* **2018**, *47*, 2431–2453.
- (7) Yang, Z.-F.; Tian, Y.-M.; Zhang, W.-Y.; Chen, P.; Li, H.-F.; Zhang, Y.-Q.; Sun, W.-B. High local coordination symmetry around the spin center and the alignment between magnetic and symmetric axes together play a crucial role in single-molecule magnet performance. *Dalton Trans.* **2019**, *48*, 4931–4940.
- (8) Fondo, M.; Corredoira-Vázquez, J.; García-Deibe, A. M.; Gómez-Coca, S.; Ruiz, E.; Sanmartín-Matalobos, J. Dysprosium-based complexes with a flat pentadentate donor: a magnetic and ab initio study. *Dalton Trans.* **2020**, *49*, 8389–8401.
- (9) (a) Ding, Y.-S.; Han, T.; Zhai, Y.-Q.; Reta, D.; Chilton, N. F.; Winpenny, R. E. P.; Zheng, Y.-Z. A study of magnetic relaxation in dysprosium(III) single-molecule magnets. *Chem. - Eur. J.* **2020**, *26*, 5893–5902. (b) Yu, K.-X.; Kragoskow, J. G. C.; Ding, Y.-S.; Zhai, Y.-Q.; Reta, D.; Chilton, N. F.; Zheng, Y.-Z. Enhancing magnetic hysteresis in single-molecule magnets by ligand functionalization. *Chem* **2020**, *6*, 1777–1793.
- (10) Canaj, A. B.; Dey, S.; Regincós Martí, E.; Wilson, C.; Rajaraman, G.; Murrie, M. Insight into D_{6h} symmetry: targeting strong axiality in stable dysprosium(III) hexagonal bipyramidal single-ion magnets. *Angew. Chem., Int. Ed.* **2019**, *58*, 14146–14151.
- (11) (a) Li, Z.-H.; Zhai, Y.-Q.; Chen, W.-P.; Ding, Y.-S.; Zheng, Y.-Z. Air-stable hexagonal bipyramidal dysprosium(III) single-ion magnets with nearly perfect D_{6h} local symmetry. *Chem. - Eur. J.* **2019**, *25*, 16219–16224. (b) Ding, X.-L.; Zhai, Y.-Q.; Han, T.; Chen, W.-P.; Ding, Y.-S.; Zheng, Y.-Z. A local D_{4h} symmetric dysprosium(III) single-molecule magnet with an energy barrier exceeding 2000 K. *Chem. - Eur. J.* **2021**, *27*, 2623–2627.
- (12) Pedersen, K. S.; Sørensen, M. A.; Bendix, J. Fluoride-coordination chemistry in molecular and low-dimensional magnetism. *Coord. Chem. Rev.* **2015**, *299*, 1–21.
- (13) Zhou, Q.; Yang, F.; Liu, D.; Peng, Y.; Li, G.; Shi, Z.; Feng, S. Synthesis, structures, and magnetic properties of three fluoride-bridged lanthanide compounds: effect of bridging fluoride ions on magnetic behaviors. *Inorg. Chem.* **2012**, *51*, 7529–7536.
- (14) Brunet, G.; Habib, F.; Korobkov, I.; Murugesu, M. Slow magnetic relaxation observed in dysprosium compounds containing unsupported near-linear hydroxo- and fluoro-bridges. *Inorg. Chem.* **2015**, *54*, 6195–6202.
- (15) Norel, L.; Darago, L. E.; Le Guennic, B.; Chakarawet, K.; Gonzalez, M. I.; Olshansky, J. H.; Rigaut, S.; Long, J. R. A terminal fluoride ligand generates axial magnetic anisotropy in dysprosium complexes. *Angew. Chem., Int. Ed.* **2018**, *57*, 1933–1938.
- (16) Huo, Y.; Chen, Y.-C.; Wu, S.-G.; Liu, J.-L.; Jia, J.-H.; Chen, W.-B.; Wang, B.-L.; Zhang, Y.-Q.; Tong, M.-L. Effect of bridging ligands on magnetic behavior in dinuclear dysprosium cores supported by polyoxometalates. *Inorg. Chem.* **2019**, *58*, 1301–1308.
- (17) Canaj, A. B.; Singh, M. K.; Regincós Martí, E.; Damjanovic, M.; Wilson, C.; Céspedes, O.; Wernsdorfer, W.; Rajaraman, G.; Murrie, M. Boosting axiality in stable high-coordinate Dy(III) single-molecule magnets. *Chem. Commun.* **2019**, *55*, 5950–5953.
- (18) Ling, B.-K.; Zhai, Y.-Q.; Han, J.; Han, T.; Zheng, Y.-Z. A stable dysprosium(III) complex with a terminal fluoride ligand showing high resolution luminescence and slow magnetic relaxation. *Dalton Trans.* **2020**, *49*, 6969–6973.
- (19) Hojorot, M.; Al Sabea, H.; Norel, L.; Bernot, K.; Roisnel, T.; Gendron, F.; Le Guennic, B.; Trzop, E.; Collet, E.; Long, J. R.; Rigaut, S. Hysteresis photomodulation via single-crystal-to-single-crystal isomerization of a photochromic chain of dysprosium single-molecule magnets. *J. Am. Chem. Soc.* **2020**, *142*, 931–936.
- (20) Fondo, M.; Corredoira-Vázquez, J.; García-Deibe, A. M.; Sanmartín-Matalobos, J.; Reta, D.; Colacio, E. Eight coordinated mononuclear dysprosium complexes of heptadentate aminophenol ligands: the influence of the phenol substituents and the ancillary donors on the magnetic relaxation. *Dalton Trans.* **2021**, *50*, 15878–15887.
- (21) Yang, L.-W.; Liu, S.; Wong, E.; Rettig, S. J.; Orvig, C. Complexes of trivalent metal ions with potentially heptadentate N₄O₃ Schiff base and amine phenol ligands of varying rigidity. *Inorg. Chem.* **1995**, *34*, 2164–2178.
- (22) Fondo, M.; Corredoira-Vázquez, J.; García-Deibe, A. M.; Sanmartín-Matalobos, J.; Amozá, M.; Botas, A. M. P.; Ferreira, R. A. S.; Carlos, L. D.; Colacio, E. Field-induced slow magnetic relaxation and luminescence thermometry in a mononuclear ytterbium complex. *Inorg. Chem. Front.* **2020**, *7*, 3019–3029.
- (23) (a) Llunell, M.; Casanova, D.; Cirera, J.; Boffill, J. M.; Alemany, P.; Alvarez, S.; Pinsky, M.; Avnir, D. D. *SHAPE v1.1b*; Barcelona, 2005. (b) Ruiz-Martínez, A.; Casanova, D.; Alvarez, S. Polyhedral structures with an odd number of vertices: nine-coordinate metal compounds. *Chem. - Eur. J.* **2008**, *14*, 1291–1303. (c) Llunell, M.; Casanova, D.; Cirera, J.; Alemany, P.; Alvarez, S. *SHAPE: Program for the Stereochemical Analysis of Molecular Fragments by Means of Continuous Shape Measures and Associated Tools*; University of Barcelona: Barcelona, Spain, 2010.
- (24) (a) Fondo, M.; Corredoira-Vázquez, J.; García-Deibe, A. M.; Sanmartín-Matalobos, J.; Herrera, J. M.; Colacio, E. Designing ligands to isolate ZnLn and Zn₂Ln complexes: field-induced single-ion magnet behavior of the ZnDy, Zn₂Dy, and Zn₂Er analogues. *Inorg. Chem.* **2017**, *56*, 5646–5656. (b) Fondo, M.; Corredoira-Vázquez, J.; Herrera-Lanzós, A.; García-Deibe, A. M.; Sanmartín-Matalobos, J.; Herrera, J. M.; Colacio, E.; Nuñez, C. Improving the SMM and luminescence properties of lanthanide complexes with LnO₂ cores in the presence of ZnII: an emissive Zn₂Dy single ion magnet. *Dalton Trans.* **2017**, *46*, 17000–17009. (c) Fondo, M.; Corredoira-Vázquez, J.; García-Deibe, A. M.; Sanmartín-Matalobos, J.; Gómez-Coca, S.; Ruiz, E.; Colacio, E. Slow magnetic relaxation in dinuclear dysprosium and holmium phenoxide bridged complexes: a Dy₂ single molecule magnet with a high energy barrier. *Inorg. Chem. Front.* **2021**, *8*, 2532–2541.
- (25) Deacon, G. B.; Evans, D. J.; Junk, P. C.; Lork, E.; Mews, R.; Zemva, B. Stabilising small clusters: synthesis and characterisation of thermolabile [Gd₄F₇(15-crown-5)₄][AsF₆]₅·6SO₂. *Dalton Trans.* **2005**, 2237–2238.

- (26) Allen, F. H. The Cambridge Structural Database: a quarter of a million crystal structures and rising. *Acta Crystallogr., Sect. B: Struct. Sci.* **2002**, *58*, 380–388.
- (27) Gorbunov, D. K.; Kizhlo, M. R.; Pushkina, G. Y.; Spridonov, F. M.; VShatskii, M. X-ray diffraction study on fluorideoxalates hydrates of the yttrium group. *Kristallografiya* **1988**, *33*, 618–620.
- (28) Chilton, N. F.; Anderson, R. P.; Turner, L. D.; Soncini, A.; Murray, K. S. PHI: A powerful new program for the analysis of anisotropic monomeric and exchange-coupled polynuclear *d*- and *f*-block complexes. *J. Comput. Chem.* **2013**, *34*, 1164–1175.
- (29) Roy, L. E.; Hughbanks, T. Magnetic coupling in dinuclear Gd complexes. *J. Am. Chem. Soc.* **2006**, *128*, 568–575.
- (30) Fomina, I. G.; Dolgushin, F. M.; Koroteev, P. S.; Mantrova, Y. V.; Korshunov, V. M.; Taydakov, I. V.; Bogomyakov, A. S.; Fedin, M. V.; Zavorotny, Y. S.; Eremanko, I. L. Binuclear gadolinium(III) pivalates with 4,7-diphenyl-1,10-phenanthroline: synthesis, structure, thermal behavior, magnetic and photoluminescence properties. *Eur. J. Inorg. Chem.* **2021**, *2021*, 464–472.
- (31) Garlatti, E.; Chiesa, A.; Bonfà, P.; Macaluso, E.; Onuorah, I. J.; Parmar, V. S.; Ding, Y.-S.; Zheng, Y.-Z.; Giansiracusa, M. J.; Reta, D.; Pavarini, E.; Guidi, T.; Mills, D. P.; Chilton, N. F.; Winpenny, R. E. P.; Santini, P.; Carretta, S. A cost-effective semi-ab initio approach to model relaxation in rare-earth single-molecule magnets. *J. Phys. Chem. Lett.* **2021**, *12*, 8826–8832.
- (32) Briganti, M.; Santanni, F.; Tesi, L.; Totti, F.; Sessoli, R.; Lunghi, A. A complete ab initio view of Orbach and Raman spin–lattice relaxation in a dysprosium coordination compound. *J. Am. Chem. Soc.* **2021**, *143*, 13633–13645.
- (33) (a) Evangelisti, M.; Brechin, E. A. Recipes for enhanced molecular cooling. *Dalton Trans.* **2010**, *39*, 4672–4676. (b) Sharples, J. W.; Collison, D. Coordination compounds and the magnetocaloric effect. *Polyhedron* **2013**, *54*, 91–103. (c) Liu, J.-L.; Chen, Y.-C.; Guo, F.-S.; Tong, M. L. Recent advances in the design of magnetic molecules for use as cryogenic magnetic coolants. *Coord. Chem. Rev.* **2014**, *281*, 26–49. (d) Zheng, Y. Z.; Zhou, G. J.; Zheng, Z.; Winpenny, R. E. P. Molecule-based magnetic coolers. *Chem. Soc. Rev.* **2014**, *43*, 1462–1475. (e) Pavlishchuk, A. V.; Pavlishchuk, V. V. Principles for creating “molecular refrigerators” derived from Gadolinium(III) coordination compounds: a review. *Theor. Exp. Chem.* **2020**, *56*, 1–25.
- (34) Tocado, L.; Palacios, E.; Burriel, R. Entropy determinations and magnetocaloric parameters in systems with first-order transitions: study of MnAs. *J. Appl. Phys.* **2009**, *105*, No. 093918.
- (35) (a) Aravena, D.; Ruiz, E. Shedding light on the single-molecule magnet behavior of mononuclear Dy^{III} complexes. *Inorg. Chem.* **2013**, *52*, 13770–13778. (b) Gómez-Coca, S.; Aravena, D.; Morales, R.; Ruiz, E. Large magnetic anisotropy in mononuclear metal complexes. *Coord. Chem. Rev.* **2015**, *289–290*, 379–392.
- (36) Leng, J.-D.; Liu, J.-L.; Lin, W.-Q.; Gómez-Coca, S.; Aravena, D.; Ruiz, E.; Tong, M. L. Unprecedented ferromagnetic dipolar interaction in a dinuclear holmium(III) complex: a combined experimental and theoretical study. *Chem. Commun.* **2013**, *49*, 9341–9343.
- (37) Sheldrick, G. M. SADABS, Area-Detector Absorption Correction; Siemens Industrial Automation, Inc.: Madison, WI, 2001.
- (38) (a) Sheldrick, G. M. SHELXT-Integrated Space-Group and Crystal-Structure Determination. *Acta Crystallogr., Sect. A: Found. Adv.* **2015**, *71*, 3–8. (b) Sheldrick, G. M. Crystal structure refinement with SHELXL. *Acta Crystallogr., Sect. C: Struct. Chem.* **2015**, *71*, 3–8.
- (39) Neese, F.; Wennmohs, F.; Becker, U.; Riplinger, C. The ORCA quantum chemistry program package. *J. Chem. Phys.* **2020**, *152*, No. 224108.
- (40) (a) Dolg, M.; Stoll, H.; Preuss, H. Energy-adjusted ab initio pseudopotentials for the rare earth elements. *J. Chem. Phys.* **1989**, *90*, 1730–1734. (b) Dolg, M.; Stoll, H.; Savin, A.; Preuss, H. Energy-adjusted pseudopotentials for the rare earth elements. *Theor. Chim. Acta* **1989**, *75*, 173–194. (c) Dolg, M.; Stoll, H.; Preuss, H. A combination of quasirelativistic pseudopotential and ligand field calculations for lanthanoid compounds. *Theor. Chim. Acta* **1993**, *85*, 441–450.
- (41) (a) Weigend, F.; Ahlrichs, R. Balanced basis sets of split valence, triple zeta valence and quadruple zeta valence quality for H to Rn: Design and assessment of accuracy. *Phys. Chem. Chem. Phys.* **2005**, *7*, 3297–3305. (b) Weigend, F. Accurate Coulomb-fitting basis sets for H to Rn. *Phys. Chem. Chem. Phys.* **2006**, *8*, 1057–1065. (c) Hellweg, A.; Hattig, C.; Hofener, S.; Klopper, W. Optimized accurate auxiliary basis sets for RI-MP2 and RI-CC2 calculations for the atoms Rb to Rn. *Theor. Chem. Acc.* **2007**, *117*, 587–597. (d) Chmela, J.; Harding, M. E. Optimized auxiliary basis sets for density fitted post-Hartree–Fock calculations of lanthanide containing molecules. *Mol. Phys.* **2018**, *116*, 1523–1538.
- (42) (a) Chibotaru, L. F.; Ungur, L.; Soncini, A. The origin of nonmagnetic Kramers doublets in the ground state of dysprosium triangles: evidence for a toroidal magnetic moment. *Angew. Chem., Int. Ed.* **2008**, *47*, 4126–4129. (b) Chibotaru, L. F.; Ungur, L.; Aronica, C.; Elmoll, H.; Pilet, G.; Luneau, D. Structure, magnetism, and theoretical study of a mixed-valence Co₃^{II}Co₄^{III} heptanuclear wheel: lack of SMM behavior despite negative magnetic anisotropy. *J. Am. Chem. Soc.* **2008**, *130*, 12445–12455. (c) Ungur, L.; Van den Heuvel, W.; Chibotaru, L. F. Ab initio investigation of the non-collinear magnetic structure and the lowest magnetic excitations in dysprosium triangles. *New J. Chem.* **2009**, *33*, 1224–1230.
- (43) Ungur, L.; Chibotaru, L. F. Strategies toward high-temperature lanthanide-based single-molecule magnets. *Inorg. Chem.* **2016**, *55*, 10043–10056.
- (44) Blum, V.; Gehrke, R.; Hanke, F.; Havu, P.; Havu, V.; Ren, X.; Reuter, K.; Scheffler, M. Ab initio molecular simulations with numeric atom-centered orbitals. *Comput. Phys. Commun.* **2009**, *180*, 2175–2196.
- (45) Becke, A. D. Density-functional thermochemistry. III. The role of exact exchange. *J. Chem. Phys.* **1993**, *98*, 5648–5652.
- (46) (a) Ruiz, E.; Cano, J.; Alvarez, S.; Alemany, P. Broken symmetry approach to calculation of exchange coupling constants for homobinuclear and heterobinuclear transition metal complexes. *J. Comput. Chem.* **1999**, *20*, 1391–1400. (b) Ruiz, E.; Alvarez, S.; Cano, J.; Polo, V. About the calculation of exchange coupling constants using density-functional theory: the role of the self-interaction error. *J. Chem. Phys.* **2005**, *123*, No. 164110.